Size- and Spatially-Controlled Nanocrystals Reveal Density-Independent Ostwald Ripening Phenomena in Catalyst Deactivation
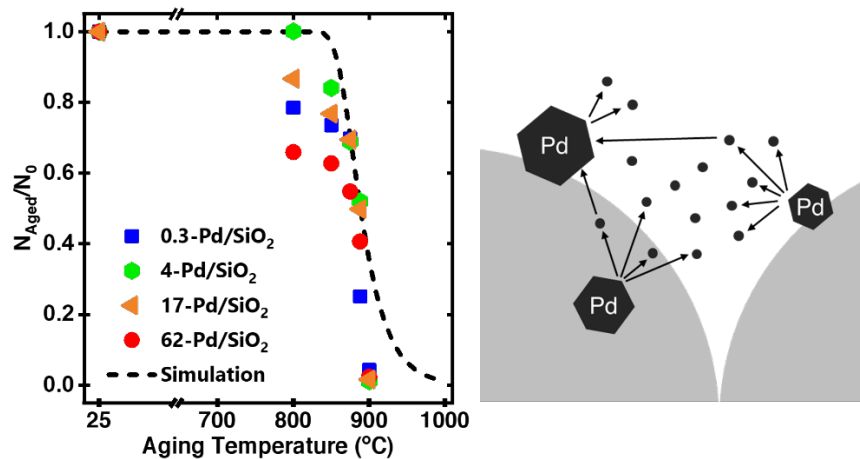
Authors: Emmett D. Goodman[1], Evan Z. Carlson[1], Elisabeth M. Dietze[2], Nadia Tahsini[1], Arun Johnson[1], Aisulu Aitbekova[1], Temy Nguyen Taylor[1], Philipp N. Plessow[2], Matteo Cargnello[1]*

[1]Department of Chemical Engineering and SUNCAT Center for Interface Science and Catalysis, Stanford University, Stanford CA, 94305, USA.
[2]Institute of Catalysis Research and Technology, Karlsruhe Institute of Technology, Hermann-von-Helmholtz-Platz 1, D-76344 Eggenstein-Leopoldshafen, Germany.

*Correspondence to: mcargnello@stanford.edu.

Significance Statement:

This work demonstrates how size and density-controlled nanocrystals (NCs) reveal important dynamics behind how supported catalysts sinter, a universal deactivation mechanism in heterogeneous catalysis, and unequivocally identifies Ostwald ripening as the cause. Counterintuitively, we observe that different nanocrystal sizes begin to grow at the same temperature. Subsequently, atomic ripening processes start, which is proven via the emergence of smaller nanocrystals, something possible to observe only with size-controlled nanocrystals. By controlling and measuring changes in nanocrystal density, we find growth to be independent of nanocrystal spatial arrangement, and in quantitative agreement with simulations of vapor-phase atomic exchange between nanocrystals that can predict the growth processes of other metals.

Abstract:

A major aim in the field of heterogeneous catalysis is the development of stable materials for high-temperature applications. Although the growth of small and active nanocrystals into less active aggregates is universal in catalyst deactivation, the mechanisms governing nanocrystal growth remain elusive. Utilizing colloidally-synthesized powder catalysts with controlled nanocrystal sizes, spatial arrangements and support geometry in Pd/SiO_2 systems, we conclusively identify Ostwald ripening processes and the atomic nature of nanocrystal growth through the emergence of smaller nanocrystals. By controlling and tracking nanocrystal density, we observe the most significant nanocrystal sintering processes to be independent of nanocrystal spatial distribution. This observation is in quantitative agreement with changes in nanocrystal density produced by simulating atomic exchange via metal vaporization processes. Using model colloidal catalysts, we extend our analysis to explain the unusually high-temperature stability of Au/SiO_2 materials up to 800 °C.

Catalyst stability is critically important in the development of industrially-relevant materials, yet is underemphasized in academic research (1). In many applications, high-temperature catalyst deactivation leads to decreased activity, changed selectivity, and overall loss of productivity due to downtime associated with catalyst reactivation or replacement (2, 3). When reactivation is not possible, catalyst deactivation drives utilization of large quantities of catalytic material to ensure effective catalysis throughout the material's application. This is the case in emissions control applications, where catalyst deactivation is responsible for the use of grams of noble metals to ensure effective catalysis throughout the lifetime of the catalytic converter (4).

In powder catalysts, one of the most common and severe causes of deactivation is due to lost reactive surface area caused by particle growth. This process is known as catalyst sintering. Two mechanisms have been proposed: Ostwald ripening, or the exchange of atoms between stationary nanocrystals; and particle migration and coalescence, the collision and fusion of entire nanocrystals (3, 5). In the literature, there is a lack of experimental methods to distinguish between these mechanisms. *In-situ* microscopy offers a promising approach, but is low-throughput, requires controlled conditions, and extreme care must be taken to avoid spurious effects of the high-energy electron beam (6). Additionally, the study of evolving particle size distributions in polydisperse catalysts has been identified as fruitless (7). Approaches involving kinetic modeling may provide insight, but incorrect assumptions can create significant errors (8). In conclusion, it has been challenging to identify which mechanism of deactivation is active in supported catalysts, thus hampering the rational design of stable catalysts.

To combat any potential sintering mechanism, researchers are continuously developing novel catalyst schemes in attempts to enhance catalyst stability. Common nanostructured motifs include encapsulation (9–13), nanocrystal embedding in nanochannels (14–16), and nanocrystal entrenchment into nanobowls or other high-surface-area supports (17, 18). Nanostructured geometries aim to physically separate particles to minimize interparticle interactions and maximize particle stability. However, such schemes often result in decreased overall activity due to mass-transfer limitations or reduced reactive surface area. A description of the specific sintering processes would allow for the intelligent design of nanostructures which target a specific deactivation mechanism.

In this work, by combining colloidally-synthesized powder catalysts and quantitative simulation studies, we provide a new fundamental understanding of catalyst stability in supported

systems. By precisely controlling nanocrystal size (3.0, 9.1, and 15.8 nm) and nanocrystal density (from 2 NC μm^{-2} to 367 NC μm^{-2}) we uncover the unique size- and density-dependences of particle growth processes. Our results demonstrate that nanocrystal growth is governed by density-independent Ostwald ripening, which is in quantitative agreement with simulations of a metallic vapor-phase sintering process. However, although vapor-phase simulations match experiments well across materials, it remains challenging to completely rule out small contributions from surface atomic processes. Identification of Ostwald ripening was only possible through size-controlled nanocrystal catalysts, proving the emergence of populations of smaller nanocrystals during high-temperature aging. We find nanocrystal growth to be independent of nanocrystal spatial distribution, suggesting atomic emission as the critical process controlling nanocrystal growth. Finally, we demonstrate that simulations of vapor-phase atomic exchange also predict the behavior of Au/SiO$_2$ catalysts, which maintain unusually remarkable stability up to 800 ºC.

Results and discussion

Synthesis and Characterization of Well-Defined Nanocrystal Ensembles. In order to disentangle the effects of nanocrystal size and spatial distribution on catalyst stability, we used a colloidal assembly approach where pre-formed Pd or Au nanocrystals were deposited onto pre-formed SiO$_2$ spheres. The key advantages of this colloidal building-block approach are: (1) a highly uniform active phase which allows probing of size-dependent sintering properties; (2) well-defined initial particle sizes, which allow particle size measurements to indicate sintering mechanism (vide infra); and (3) independent control of the size and spatial distribution of NCs, to study the effect of spatial parameters on catalyst stability. Here, we synthesized size-controlled 3.0 ± 0.3 nm, 9.1 ± 0.5 nm, and 15.8 ± 1.3 nm Pd nanocrystals as active phases (**Figure 1a-c**), and monodisperse 232 nm Stober SiO$_2$ spheres as the supporting oxide phase. Controlled assembly of Pd nanocrystals onto colloidal SiO$_2$ was performed by impregnation in solution, such that Pd was well-dispersed on the surface of each SiO$_2$ sphere (**Figures 1d-f, Figures S1-S3**). Although transmission electron microscopy (TEM) measurements may show overlap between Pd NCs, this effect is due to the 2D projection nature of microscopy images for particles lying on opposite sides of the SiO$_2$ spheres. High-angular annular dark field scanning tunneling electron microscopy (HAADF-STEM) tomography demonstrates the random distribution of Pd NCs on the overall SiO$_2$

surface (**Figure S4**). Measurements of Pd nanocrystal size as-synthesized and after assembly onto the SiO$_2$ surface confirm the uniformity of the Pd phase, although a slight decrease in size is observed due to different wetting properties of Pd on carbon with respect to silica (**Figure 1g-i**). Pd loading and additional characterization for each catalyst are reported in **Table S1**.
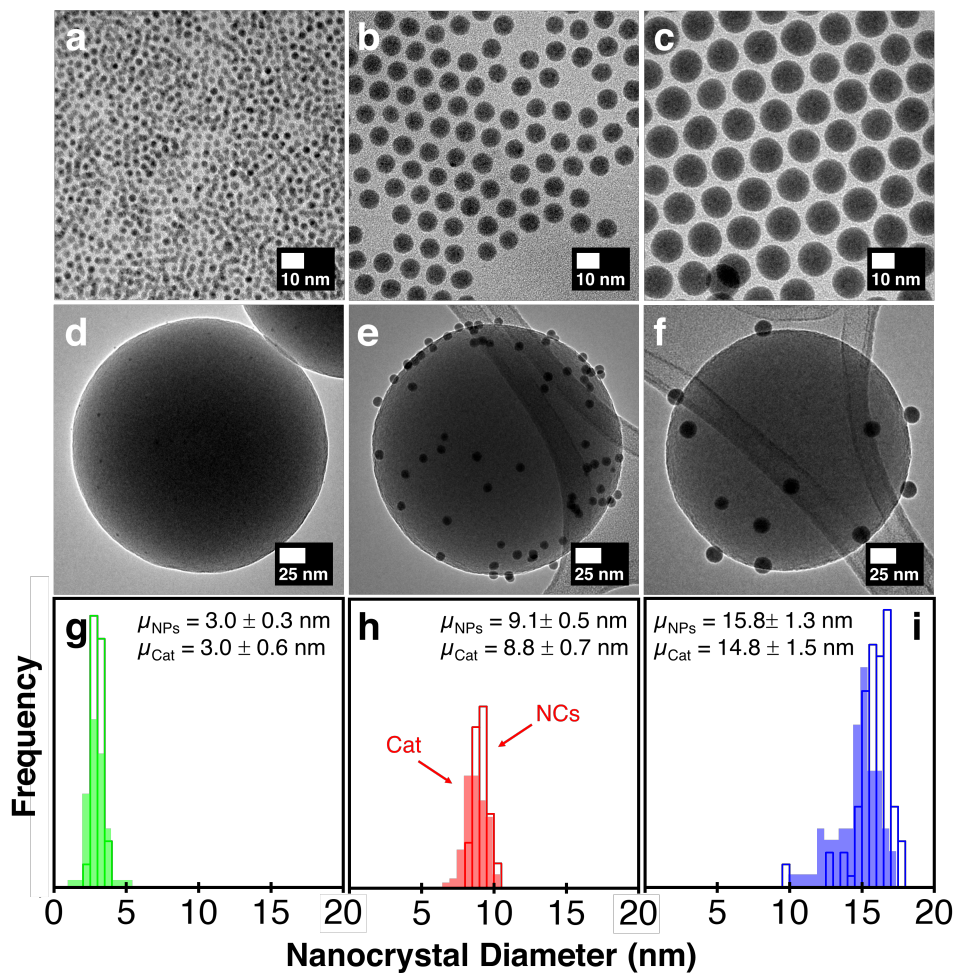
Figure 1. **Size-Controlled Nanocrystal Catalysts.** Transmission electron microscopy (TEM) images of three sizes of (a-c) as-synthesized colloidal Pd nanocrystals and (d-f) corresponding SiO$_2$-supported Pd nanocrystals. Particle size distributions (g-i) of as-synthesized nanocrystal (open bars) and SiO$_2$-supported nanocrystals (closed bars). Mean values and standard deviations shown for as-synthesized nanocrystals (μ_{NCs}) and SiO$_2$-supported nanocrystals (μ_{Cat}).

Thermal Stability Studies. The prepared materials were used to study the size-dependent Pd stability after calcination in air. The SiO$_2$ support spheres are stable in air up to at least 925 °C and

therefore remain stable under the conditions investigated in this work. For each catalyst, we measure the mean nanocrystal diameter after aging at increasing temperature (**Figure 2**). Surprisingly, for all samples regardless of Pd particle size, the average nanocrystal diameter does not change appreciably until the relatively high temperature of 875 °C, demonstrating the stability of the Pd/SiO$_2$ materials. Although an increase in nanocrystal size was observed between 25 °C and 800 °C, this slight growth is consistent with the oxidative expansion of the colloidally-synthesized Pd NCs with the metal phase converting to PdO (**Table S2**). Between 888 °C and 900 °C, the mean diameter of the 3.0 nm and 8.8 nm samples increased dramatically to ~30 nm. The fact that these samples show particle growth at approximately the same temperature is surprising given that smaller particles are usually considered having a much higher driving force to sinter due to their higher surface energy (19). Once 3.0 nm Pd begins to sinter, the number of NCs per SiO$_2$ sphere dramatically falls, and very few yet large Pd aggregates were observable. Although the 14.7 nm sample also produced numerous larger aggregates between 888 °C and 900 °C, the mean particle diameter slightly decreased, which gives fundamental insight into the mechanism of particle growth (vide infra). Overall, all NC sizes produce very large sintered aggregates at 888 °C, and this temperature represents a critical turning point in the stability of the Pd/SiO$_2$ materials.
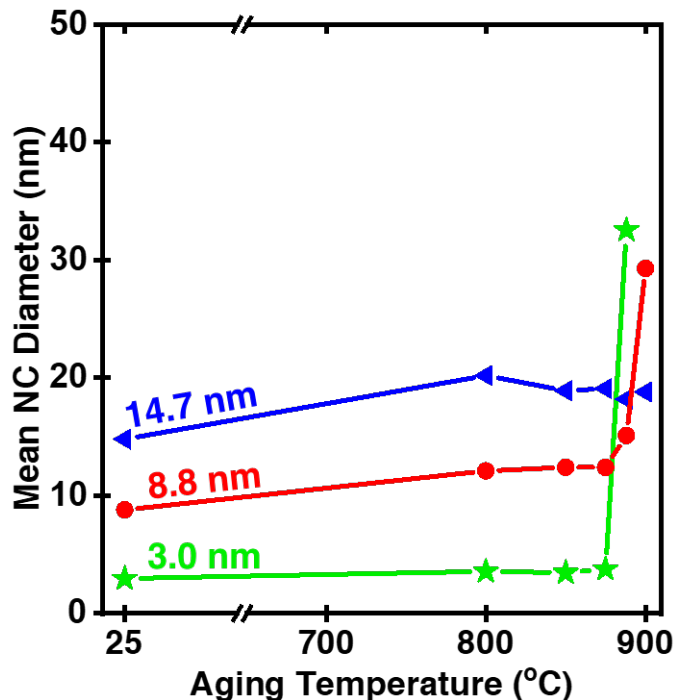
Figure 2. Size-Dependent Stability of Pd/SiO₂ Materials. Mean NC diameter versus aging temperature for 3.0 nm, 8.8 nm, and 14.7 nm Pd/SiO₂ catalysts.

Bulk characterization techniques were used on the 8.8 nm Pd/SiO₂ sample to understand why sintering rapidly onset at 888 °C. Attenuated Total Reflectance Fourier-Transform Infrared Spectroscopy (ATR-FTIR) measurements were performed to understand if SiO₂ chemistry governed the unique stability of the Pd/SiO₂ catalysts (**Figure S5**). However, no obvious changes in surface chemistry of SiO₂ were observed upon reaching 875 °C, suggesting that changes in the support are not determining the observed stability behavior. We therefore studied changes in the Pd oxidation state in order to understand its contribution to the observed sintering behavior. According to procedures developed to preserve the oxidation state in Pd catalysts, the 8.8 nm Pd/SiO₂ was heated to either 875 °C or 900 °C for 5 h in static air, and rapidly cooled down for analysis to freeze the state of the Pd particles (20). High resolution TEM (HRTEM) analysis was performed to understand the oxidation state of the material during the sintering process (**Figure 3a**). While at 875 °C we observe mostly PdO, after 900 °C aging we observe the emergence of metallic Pd in sintered aggregates larger than 25 nm in diameter (**Figure 3b**). Additional proof of

the relationship between oxidation state and stability was obtained via X-ray diffraction (**Figure 3c**). Similar to TEM analysis, while we only observe PdO after aging at 875 °C, we find the emergence of metallic Pd after aging at 900 °C. The fact that metallic Pd is observed only when sintering has occurred indicates that metallic Pd is necessary for sintering of the catalyst. Further proof is obtained by performing in-situ temperature programmed reduction experiments, where particle growth is only observed after PdO is reduced to Pd (**Figure S6**).
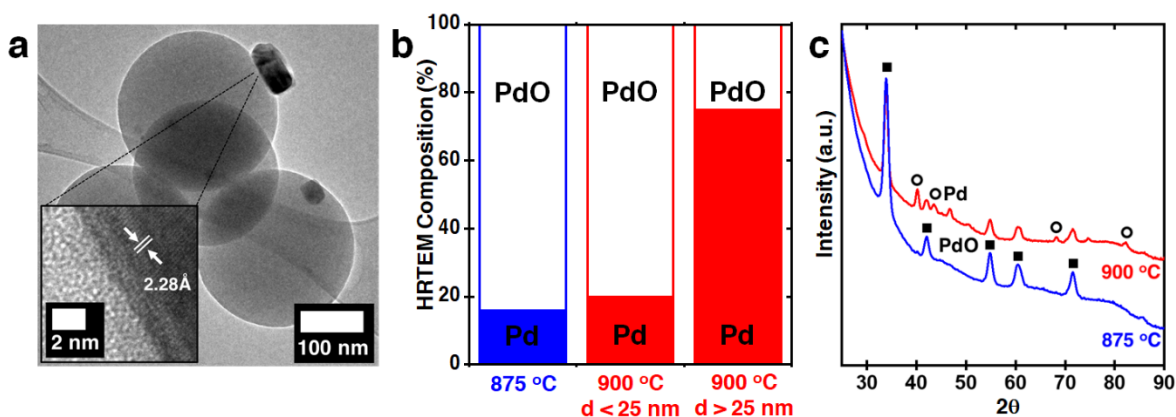
Figure 3. Critical Sintering Temperature and the PdO-Pd Phase Transition. (a) TEM image of 8.8 nm Pd/SiO_2 catalyst after aging and rapid cool-down from 900 °C. Inset: Representative HR-TEM image and lattice indexing indicating metallic Pd phase. (b) Lattice imaging analysis and statistics of 50 total HRTEM images of 8.8 nm Pd/SiO_2 catalyst after aging at 875 °C and 900 °C and rapid cool-down. (c) From the same materials, X-ray diffractograms.

Although we implicate the metallic Pd state in the sintering mechanism, it remains unclear whether Ostwald ripening or particle migration and coalescence has led to particle growth. In order to answer this question, detailed particle size analysis was performed after different aging treatments for the 14.7 nm Pd/SiO_2 sample. After aging at 800 °C or 900 °C for 5 hours in static air, 200 particles were measured along the maximum chord as observed via TEM (**Figure 4, S7**), but analysis of projected nanocrystal area yields the same conclusions (**Figure S8**). Overall, a shift of the distribution center of mass from ~19 nm to ~16 nm is observed, and a compensatory evolution of much larger 40-80 nm aggregates appear. Most importantly, after aging at 900 °C we observe the emergence of NCs with an average size of less than 10 nm, smaller than the smallest particles

present in the 800 °C aged sample, and smaller than the original Pd NCs. The emergence of small NCs is conclusive evidence of Ostwald ripening, where particle size decrease is due to atomic emission and recapture by larger particles, and is uniquely demonstrated by using size-controlled nanocrystal catalysts. On the other hand, particle coalescence processes could only generate nanocrystals larger than the original nanocrystal building blocks, and would lead to a bimodal size distribution. Furthermore, the emergence of smaller nanocrystals, without the entire disappearance of nanocrystals, explains the decrease in NC diameter observed in **Figure 2** for the sample containing large nanocrystals between 800 °C and 900 °C. A schematic inset in **Figure 4a** illustrates how atomic exchange between nanocrystals leads to smaller nanocrystals.
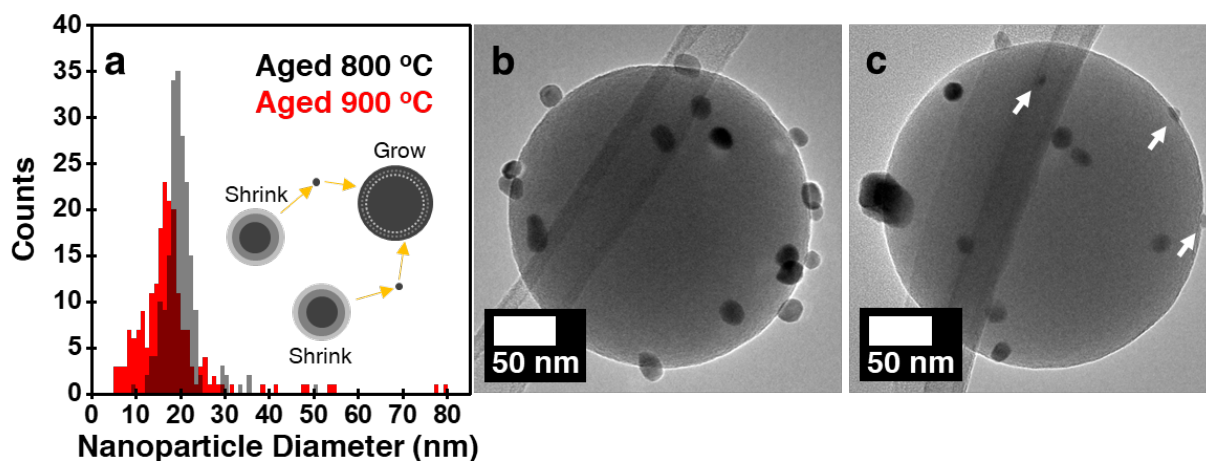
Figure 4. Particle Size Distribution Analysis Reveals Atomic Ripening. Particle size distributions of 14.7 nm Pd/SiO$_2$ catalyst after aging treatments at 800 °C or 900 °C for 5 h in static air (N = 200). Inset shows schematic illustrating atomic growth and decay of nanocrystals. Representative TEM image of catalysts after aging in static air for 5 hours at (b) 800 °C and (C) 900 °C.

To probe the effect of nanocrystal spatial distribution on catalyst stability, 9.1 nm Pd NCs were used to synthesize four catalysts with NC densities that vary over two orders of magnitude. Representative TEM images of the four materials are shown in **Figure 5a-d**, where we observe different NC spatial distribution but maintained NC size. The NC loadings are quantified by tallying the number of Pd NCs per SiO$_2$ sphere over many Pd/SiO$_2$ structures within a sample, and these statistics are shown in **Figure 5e-h**. Consequently, the four materials are labelled as 0.3-

Pd/SiO$_2$, 4.0-Pd/SiO$_2$, 17-Pd/SiO$_2$, and 62-Pd/SiO$_2$, after the average number of Pd NCs per SiO$_2$ sphere. By computationally simulating this random NC deposition process and modeling a large number of spheres with a given number of Pd NCs on their surface, we can calculate the distribution of nearest neighbor distances for each sample, a parameter crucial to processes where interparticle diffusion governs the material stability (**Figure S9**) (14). As the average nearest neighbor distance between NCs varies from 26 nm to 173 nm along the sample series, we expect these materials to possess different stability properties if surface diffusional processes dominate. Additionally, these Pd/SiO$_2$ composites represent localized support surfaces where particles may sinter, as there are significant barriers to atomic transfer between spheres (21). These four materials were aged for 5 h at 900 °C in static air, and representative TEM images and density statistics are shown in **Figure 5i-p**. This choice was motivated by the fact that the stability of emissions control catalysts are typically studied under oxidizing conditions at temperatures up to 900 °C (22). At this temperature, all materials show dramatic NC sintering, evidenced by increasing particle size and loss of NC density. Importantly, as NC density is lost, we observe the rise in SiO$_2$ spheres that no longer contain any NCs (**Figure S10**), demonstrating that Pd is able to traverse hundreds of nanometers, and that Pd transport is not hindered between SiO$_2$ spheres. This intersphere Pd transport is also confirmed via particle size analysis, with the emergence of very large aggregates >50 nm, suggesting that 9.1 nm Pd NCs must be sourced from numerous SiO$_2$ spheres.
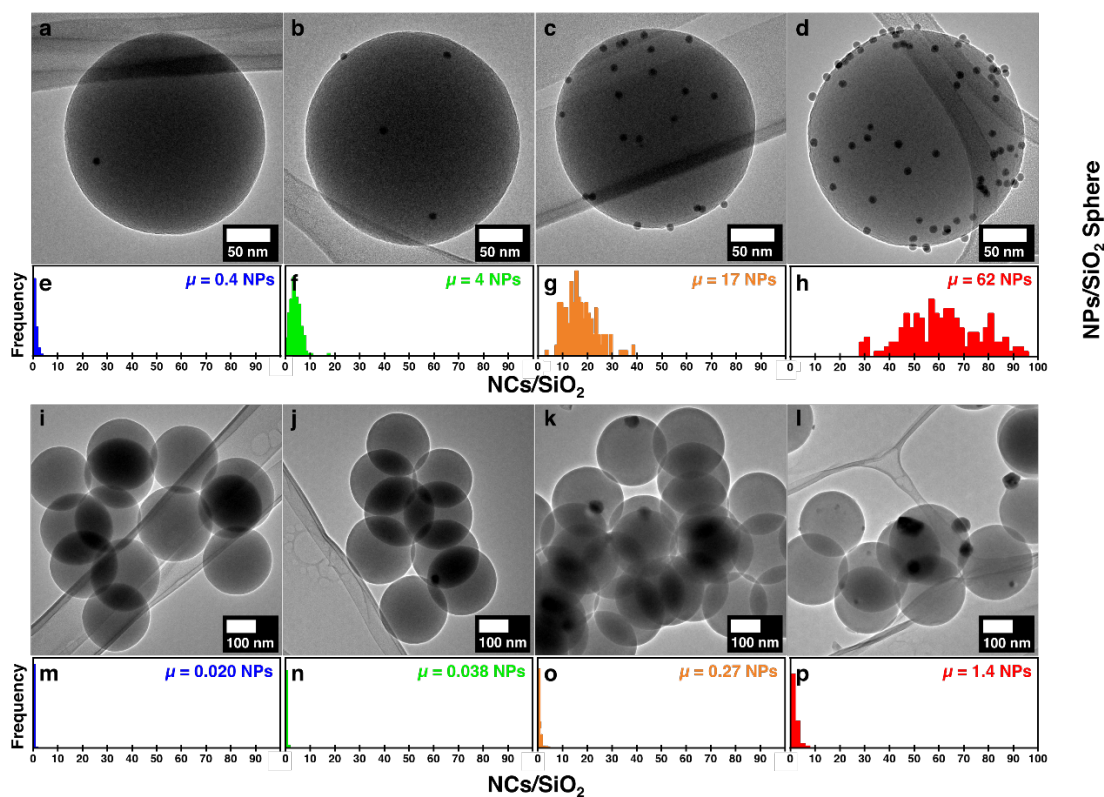
Figure 5. **Catalysts with Independent Control of NC Size and NC Density Demonstrate Density-Independent Sintering.** Representative TEM image and density statistics of 8.8 nm Pd/SiO$_2$ materials with mean NC-Pd/SiO$_2$ values of (a,e) 0.3-Pd/SiO$_2$ (b,f) 4.0-Pd/SiO$_2$ (c,g) 17-Pd/SiO$_2$ and (d,h) 62-Pd/SiO$_2$. After aging at 900 °C for 5 h in static air, representative TEM image and density statistics of (i,m) 0.3-Pd/SiO$_2$ (j,n) 4.0-Pd/SiO$_2$ (k,o) 17-Pd/SiO$_2$ and (l,p) 62-Pd/SiO$_2$.

Additional quantitative particle density analysis was performed for the four samples at various temperatures up to 900 °C, where change in NC density is represented as the post-treatment nanocrystal density divided by the original nanocrystal density (N$_{Aged}$/N$_0$) (Figure 6a). The particle density decreases slightly between 25 °C and 800 °C, and most notably for the 62-Pd/SiO$_2$ material, which experiences a 35% loss of NC density. However, this loss can be again quantitatively explained due to oxidative expansion and fusion of NCs at very close distance, where quantitative analysis reveals the formation of NC dimers (**Figure S11**). This low temperature fusion happens to a much lesser extent at lower NC densities, as nearest neighbor distances are larger. Overall, the materials maintain high nanocrystal density until ~800 °C, at which point nanocrystal density rapidly falls. Similar stability results are identified for Pd/SiO$_2$ catalysts synthesized with

commercial Davisil SiO_2, suggesting this remarkable stability is not a unique function of impurities in the SiO_2 prepared with our method, but is instead a more general phenomenon of SiO_2-supported catalysts (**Figure S17**). Surprisingly, aside from the early oxidative fusion of nearby crystallites between room temperature and 800 °C, there is no obvious trend relating how initial NC density, controllably varied in these four materials, affects aged NC density. Instead the samples follow the same trend independent of initial NC density, and all the catalysts fall onto the same curve. Density independence of NC growth means that the distance between NCs is not the most important factor for NC stability, suggesting that atomic diffusion of Pd is rapid and Pd atomic emission is the rate determining step in the Pd sintering process. A similar emission-limited process was recently observed in the case of atomic redispersion for Pd/Al_2O_3 and has been theorized in other works (6, 23). The fact that the 0.3-Pd/SiO_2 sample containing a very low density of particles sinters to such a great extent, leaving behind many empty SiO_2 spheres to form large Pd aggregates, demonstrates the large distances Pd is rapidly traveling. It is extremely challenging to find Pd aggregates in the 0.3-Pd/SiO_2 sample, with an average ratio of 1 Pd aggregate per 300 SiO_2 spheres, suggesting that Pd traverses up to 1 micron within the prolonged sintering process.

Given the remarkable high-temperature stability of the Pd/SiO_2 catalysts, and the atomic nature of the sintering process across SiO_2 spheres, a vapor-phase sintering process was hypothesized. Although little quantitative analysis of vapor-phase sintering exists in the experimental literature, significant efforts in analyzing these processes have been pursued via simulations and modeling (24). Implementing recently developed simulations for vapor-phase sintering processes, we modeled changes in nanocrystal density due to a vapor-phase sintering process of metallic Pd as a function of temperature, in the absence of any contributions from surface atomic processes or particle migration and coalescence processes. Vapor-phase ripening simulations were performed using a mean-field model for Ostwald ripening, which assumes a constant background pressure of the migrating species (25). These vapor-phase simulations are represented as a dashed line in **Figure 6a**. It is important to note that the developed vapor-phase simulation is independent of nanocrystal spatial distribution due to the assumption that Pd diffusion in the gas phase is more rapid than emission into the gas phase; this assumption is consistent with our experimental observations showing that change in nanocrystal density is independent of the initial state (Figure 6a). Sensitivity of this vapor-phase simulation to slight variations in nanocrystal surface energy are plotted in **Figure S12**. In these simulations, the Gibbs-

Thompson equation is used to model the size-dependent nanocrystal energies, and adhesion energies, while important in general, are neglected due to the known weak interactions of SiO_2 supports (26, 27). Overall, experimentally measured changes in nanocrystal density match well with its loss simulated via a vapor-phase sintering mechanism, although at high temperature, experimentally observed sintering occurs to a greater extent than those simulated in a vapor-phase process. Vapor pressure calculations of metallic Pd at 900 °C reveal that each NC emits 4 times its total volume of atoms within a 5 hour aging experiment, each NC emitting 5 atoms each second (**Figure S13**). Emitted gas-phase Pd atoms would have a root mean square velocity of 524 m s^{-1} at 900 °C, suggesting that it would take a Pd atom 442 picoseconds (ps) to travel 232 nm between SiO_2 spheres. Compared to an atomic emission rate of 5 atoms s^{-1}, it is clear that atomic emission, rather than vapor-phase or surface diffusion, is the rate-determining sintering step. A scheme of rapid vaporization of Pd across SiO_2 spheres is shown in Figure 6b.
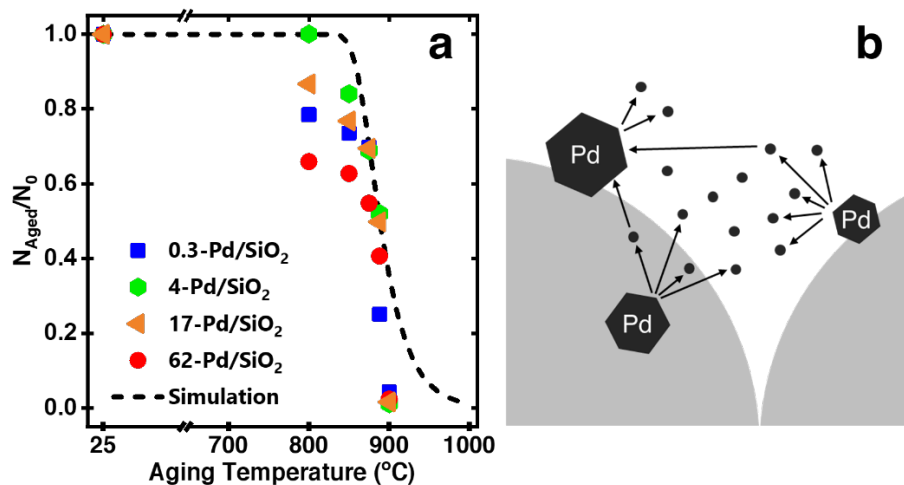
Figure 6. Tracking Nanocrystal Density and the Vapor-Phase Sintering Mechanism. (a) Changes in nanocrystal density for 8.8 nm Pd/SiO$_2$ catalysts as a function of aging temperature. Experimentally measured points are represented with symbols. The vapor phase simulation is represented by the dotted black line, which was performed according to a previously reported protocol (25). (b) Schematic illustrating vapor-phase atomic exchange between nanocrystals, which shows Pd transfer across SiO_2 spheres.

Surprisingly, the vapor-phase sintering model predicts nanocrystal growth at 700-800 °C for 3.0 nm Pd **(Figure S12)**, yet experimentally we observe stability until 875 °C **(Figure 2)**. Although these smallest nanocrystals seem to achieve stability past the vapor-phase limit, this unexpected result can be explained by understanding the role of oxidation state in the sintering process. At temperatures between 700 °C and 875 °C, particles are still oxidized as PdO, and therefore do not have sintering behavior governed by vapor phase processes of metallic Pd (28). However, when these particles reduce to metallic Pd at 888 °C, we observe rapid loss of almost all particle density, as this sample begins being dominated by atomic sintering processes. At this point, it becomes extremely challenging to observe Pd aggregates, and only 1-3 Pd aggregates were found after aging at 900 °C, although the aggregates were at least 20 nm in size. Note that although the emission-limited atomic process studied here is shown to be in quantitative agreement with NC vaporization, it remains a challenge to absolutely rule out emission-limited atomic surface processes. However, given the satisfactory match between experiments and simulations, the data suggests that atomic surface processes are likely not occurring to an extent as to dominate the nanocrystal growth process.

Au/SiO$_2$ Catalysts. To probe the generality of the vapor-phase sintering mechanism, we also studied particle growth in Au/SiO$_2$ materials. Au catalysts are heavily investigated for several applications, although catalyst stability is a well-established issue (3). Numerous nanostructured support motifs have been developed to increase the stability of Au catalysts (12, 29–34). Here, similar temperature-dependent stability studies were performed on a colloidally-synthesized Au/SiO$_2$ catalyst, where nanocrystal density was tracked against aging temperature. The average number of Au NCs per SiO$_2$ sphere was 2.2 in the as-synthesized material. Surprisingly, Au NC density remains constant up to 800 °C, at which point nanocrystal density dropped by a factor of five as temperature approached 900 °C. This data indicates that Au/SiO$_2$ materials are stable until at least 800 °C, and then they begin to undergo processes of particle growth similar to what was described for Pd. Representative TEM images of the Au/SiO$_2$ as-synthesized (**Figure 7a**) and aged at 800 °C (**Figure 7b**) demonstrate that the small size of the Au NCs was maintained even when multiple NCs coexist on the same SiO$_2$ sphere. Quantitatively, average size changes minimally, from the 7.8 nm Au starting material to 7.5 nm Au after aging (**Figure S14**). Although the high-temperature stability of this Au/SiO$_2$ may be unexpected, this stability is quantitatively predicted

via simulation of the vapor-phase sintering mechanism, which is also plotted in **Figure 7b**. Au does not form a stable oxide but remains metallic up to high temperatures, which explains why the vapor-phase mechanism in this case very well explains the behavior.
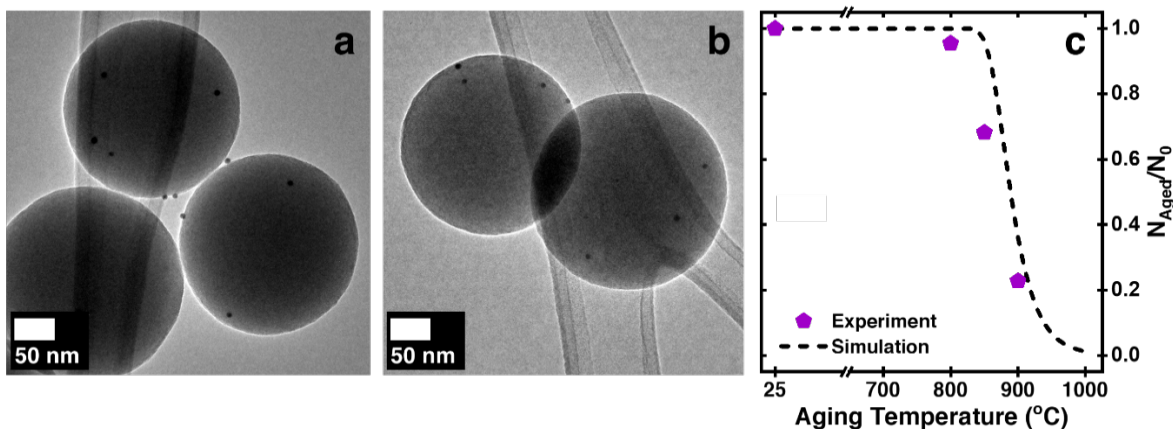
Figure 7. **Vapor-Phase Sintering of Au/SiO₂.** (a) Representative TEM images of Au/SiO₂ (a) as-synthesized and (b) after aging treatment at 800 °C for 5 h in static air. (c) Experimental and simulated NC density versus aging temperature for the Au/SiO₂ catalyst.

The high-temperature stability of the Au catalyst, which can be explained by vapor-phase sintering processes, is surprising given that the vast efforts put forth to design nanostructured Au catalysts, which would produce barriers to surface processes, but not necessarily vapor processes. We attribute previous works showing drastic sintering of Au-based catalysts to different supports or the presence of byproducts from the synthesis that could undermine Au stability with temperature. Furthermore, in many studies showing Au sintering at lower temperatures, Au NCs may be separated by trivially small distances of ~1-2 nm where processes such as directed migration of adjacent particles within such small proximities may occur (34, 35). In literature examples where control catalysts are compared to encapsulated materials, it is likely that the control material does not contain the exact same nanocrystal size distribution as the encapsulated sample, which may lead to confounding effects in understanding catalyst stability. Nevertheless, there still exist many studies toting the encapsulation of Au for enhanced stability under static calcination conditions (12, 36–38). Here we demonstrate that 'unencapsulated' Au NCs on SiO₂ maintain their stability up to 800 °C in static furnace calcination, at which point they sinter in a

process quantitatively consistent with a vapor-phase atomic mechanism. This method can therefore be generalized and extended to several other systems and understand their deactivation behavior.

Conclusions. In this work, we demonstrate how to synthesize powder catalysts with precise and independent control of nanocrystal size and nanocrystal spatial distribution. These materials are not only highly stable, but represent important tools in providing fundamental understanding and atomistic insight into catalyst sintering mechanisms. For the first time, the atomic nature of the sintering process is revealed in powder catalysts by using size-selected nanocrystals, where we observe the emergence of small nanocrystals. Nanocrystal densities are controlled and tracked throughout the aging process, and experimentally measured nanoparticle densities are in quantitative agreement with simulations based on the vapor pressure of Pd and Au metals. The work also demonstrates that appropriate conditions can stabilize metals well beyond what is reported in the literature.

Methods

Material Synthesis. Pd NCs were synthesized according to prior work (23). ~18g of SiO_2 spheres were synthesized in a scaled up batch synthesis, according to the following procedure: 72 mL MilliQ H_2O was mixed with 400 mL EtOH (Gold Shield), which was heated to 75 °C and maintained at that temperature for 15 min. Next, 67 mL of NH_4OH (28 – 30%) was added, temperature quickly fell to 65 °C, at which point 60 mL tetraethyl orthosilicate (TEOS, 98% Aldrich) was quickly added under vigorous stirring. The solution immediately turned pearly white, and the reaction was completed after 10 minutes. SiO_2 spheres were stored in solution and only isolated as a solid directly prior to use.

Extensive effort was taken to synthesize composite materials with controlled NC size and spatial distribution. In short, 1.52 mL (50 mg) of colloidal SiO_2 from the mother solution (H_2O/EtOH/NH_3) was isolated by centrifugation at 8000 rpm for 10 min. The recovered powder was dried in a centrifuge vial upside down for 10 min, and then redispersed in 15 mL toluene via sonication and vortexing. At this point, the SiO_2 spheres disperse poorly in toluene, and quickly precipitated. The powder was isolated again at 8000 rpm for 3 min, and redispersed in 35 mL of a 15 vol. % EtOH/toluene solution, which dispersed the SiO_2 well. The desired amount of Pd NPs, precipitated once with EtOH and isopropanol (IPA), was redispersed in 5 mL of toluene, and added

dropwise to the stirring SiO_2 solution over a period of 5 minutes. This dark mixture was allowed to stir for 30 min, at which point the composite materials were isolated by centrifugation at 8000 rpm for 3 min, and dried overnight at 80 °C. These materials were sieved through an 80 μm mesh prior to thermal stability testing.

Thermal Aging Experiments and Statistics. Typically, four small ceramic crucibles (each with ~5 mg of catalyst) were placed near the center of a box furnace, and all were heated simultaneously. The samples were subjected to a 3 °C min^{-1} ramp rate up to the calcination temperature, followed by a five hours isothermal treatment, and finally ramped back down at 3 °C min^{-1} to room temperature. Without further treatment, the samples were dry-loaded onto a C/Cu TEM grid for analysis. In cases where rapid cool-down was used, (i.e. Figure 3), the furnace was carefully opened, and the crucible was extracted directly with large tongs and cooled by sitting in ambient air. Control experiments demonstrated that this rapid isolation was crucial, as slow cooldown at 3 °C min^{-1} would lead to a sample that was completely oxidized. Unless noted, at least 100 SiO_2 spheres were analyzed to get density statistics, and at least 100 NCs were measured to obtain NC size statistics. 100 NCs were not able to be counted for the 3.3 nm Pd/SiO_2 sample aged at 900 °C due to the small density of NCs on the surface after sintering.

Monte Carlo Simulations of Nearest Neighbor Nanoparticle Distances (Fig S8) and Particle per Bead Distributions (Figure S13). Monte Carlo simulations were performed using standard MATLAB functions. To calculate nearest neighbor distances, an ensemble of at least one thousand SiO_2 was populated with randomly distributed nanoparticles (i.e. 4, 17, or 62 per bead), according to a known algorithm (http://mathworld.wolfram.com/SpherePointPicking.html). Next, a two-dimensional matrix of all interparticle distances (greater circle distances) across the spherical surface was calculated. For each nanoparticle, the smallest nearest neighbor distance was selected. By collecting these nearest neighbor distances for thousands of nanoparticles on thousands of spheres, a histogram of nearest neighbor distances was compiled.

Vapor-Phase Simulations

Vapor-phase ripening simulations were performed using a mean-field model for Ostwald ripening, which assumes a constant background pressure of the migrating species (25, 39). Particle-size

dependent vapor pressures were calculated using the Gibbs-Thomson equation with experimental values for both the surface free energies of Pd and Au and their temperature dependent bulk vapor pressures (see Table S3 in the supporting information). The sticking coefficient of the atoms on the metallic surfaces is assumed to be 1. The simulations were initialized with a discretized particle distribution according to a normal distribution, which is centered at the mean diameter and is cut off at values larger than 3 times the standard deviation. Experimental mean diameters and standard deviations of the SiO_2-supported nanocrystals, as indicated in Fig. 1, were used. The discretization is based on 1000 bins to ensure a smooth particle size distribution. The simulated time is 5 h with a time step that is restricted to be below 0.027 s.

Author contributions. E.G. and M.C. conceived the idea for the study. E.G. prepared the samples with contribution from E.Z.C., N.T., A.J. and T. T. E.G. and A.A. performed the XPS and TEM characterization. E.D. performed vapor-phase simulation with supervision from P.P. M.C. supervised the entire project. E.G. wrote the manuscript with contribution from all authors.

Competing financial interests. The authors declare no competing financial interests or conflicts of interest.

Additional information. Supplementary information is available in the online version of the paper. Reprints and permissions information is available online at www.nature.com/reprints. Correspondence and requests for materials should be addressed to M.C.

References.

1.   S. L. Scott, A Matter of Life(time) and Death. *ACS Catal.* **8**, 8597–8599 (2018).

2.   M. D. Argyle, C. H. Bartholomew, Heterogeneous Catalyst Deactivation and Regeneration: A Review. *Catalysts* **5**, 145–269 (2015).

3.   E. D. Goodman, J. A. Schwalbe, M. Cargnello, Mechanistic Understanding and the Rational Design of Sinter-Resistant Heterogeneous Catalysts. *ACS Catal.* **7**, 7156–7173 (2017).

4.   Robert J. Farrauto, Low-Temperature Oxidation of Methane. *Science* **337**, 659–661 (2012).

5.   T. W. Hansen, A. T. Delariva, S. R. Challa, A. K. Datye, Sintering of catalytic nanoparticles: Particle migration or ostwald ripening? *Acc. Chem. Res.* **46**, 1720–1730 (2013).

6.   S. R. Challa, *et al.*, Relating Rates of Catalyst Sintering to the Disappearance of Individual Nanoparticles during Ostwald Ripening. *J. Am. Chem. Soc.* **133**, 20672–20675 (2011).

7.   A. K. Datye, Q. Xu, K. C. Kharas, J. M. Mccarty, Particle size distributions in heterogeneous catalysts : What do they tell us about the sintering mechanism ? *Catal. Today* **111**, 59–67 (2006).

8.   S. C. Parker, C. T. Campbell, Kinetic model for sintering of supported metal particles with improved size-dependent energetics and applications to Au on TiO2 (110). *Phys. Rev. B* **75**, 035430 (2007).

9.   L. De Rogatis, *et al.*, Embedded Phases : A Way to Active and Stable Catalysts. *ChemSusChem* **3**, 24–42 (2010).

10.   Y. Xu, *et al.*, Palladium nanoparticles encapsulated in porous silica shells: An efficient and highly stable catalyst for CO oxidation. *RSC Adv.* **3**, 851–858 (2013).

11.   A. J. Forman, *et al.*, Silica-Encapsulated Pd Nanoparticles as a Regenerable and Sintering-Resistant Catalyst. *ChemCatChem* **2**, 1318–1324 (2010).

12.   P. M. Arnal, M. Comotti, F. Schuth, High-Temperature-Stable Catalysts by Hollow

Sphere Encapsulation**. *Angew. Chemie - Int. Ed.* **45**, 8224–8227 (2006).

13. S. H. Joo, *et al.*, Thermally stable Pt/mesoporous silica core-shell nanocatalysts for high-temperature reactions. *Nat. Mater.* **8**, 126–131 (2009).

14. G. Prieto, J. Zecevic, H. Friedrich, K. Jong, P. Jongh, Towards stable catalysts by controlling collective properties of supported metal nanoparticles. *Nat. Mater.* **12**, 34–39 (2013).

15. X. Yan, *et al.*, Unusual Loading-Dependent Sintering-Resistant Properties of Gold Nanoparticles Supported within Extra-large Mesopores. *Chem. Mater.* **25**, 1556–1563 (2013).

16. M. T. Bore, *et al.*, The Role of Pore Size and Structure on the Thermal Stability of Gold Nanoparticles within Mesoporous Silica. 2873–2880 (2005).

17. J. Liu, Q. Ji, T. Imai, K. Ariga, H. Abe, Sintering-Resistant Nanoparticles in Wide-Mouthed Compartments for Sustained Catalytic Performance. *Nat. Sci. Reports*, 1–8 (2017).

18. X. Yang, *et al.*, Taming the stability of Pd active phases through a compartmentalizing strategy toward nanostructured catalyst supports. *Nat. Commun.* **10**, 1–9 (2019).

19. C. T. Campbell, S. C. Parker, D. E. Starr, The Effect of Size-Dependent Nanoparticle Energetics on Catalyst Sintering. *Science* **298**, 811–814 (2002).

20. H. Xiong, *et al.*, Metastable Pd ⇔ PdO Structures During High Temperature Methane Oxidation. *Catal. Letters* **147**, 1095–1103 (2017).

21. L. DeRita, *et al.*, Structural evolution of atomically dispersed Pt catalysts dictates reactivity. *Nat. Mater.* **18**, 746–751 (2019).

22. J. G. McCarty, G. Malukhin, D. M. Poojary, A. K. Datye, Q. Xu, Thermal Coarsening of Supported Palladium Combustion Catalysts †. *J. Phys. Chem. B* **109**, 2387–2391 (2005).

23. E. D. Goodman, *et al.*, Catalyst deactivation via decomposition into single atoms and the role of metal loading. *Nat. Catal.* (2019) https:/doi.org/10.1038/s41929-019-0328-1.

24. E. M. Dietze, P. N. Plessow, Kinetic Monte Carlo Model for Gas Phase Diffusion in Nanoscopic Systems. *J. Phys. Chem. C* **122**, 11524–11531 (2018).

25. P. N. Plessow, F. Abild-Pedersen, Sintering of Pt Nanoparticles via Volatile PtO 2 : Simulation and Comparison with Experiments. *ACS Catal.* **6**, 7098–7108 (2016).

26. C. T. Campbell, Z. Mao, Chemical Potential of Metal Atoms in Supported Nanoparticles :

Dependence upon Particle Size and Support. *ACS Catal.* **7**, 8460–8466 (2017).

27.	S. Soled, Silica-supported catalysts get a new breath of life. *Science (80-.).* **350**, 1171–1172 (2015).

28.	Y. H. Chin, E. Iglesia, Elementary Steps, the Role of Chemisorbed Oxygen, and the Effects of Cluster Size in Catalytic CH4-O2 Reactions on Palladium. *J. Phys. Chem. C* **115**, 17845–17855 (2011).

29.	B. K. Min, W. T. Wallace, D. W. Goodman, Synthesis of a Sinter-Resistant , Mixed-Oxide Support for Au Nanoclusters. *J. Phys. Chem. B*, 14609–14615 (2004).

30.	A. Beck, *et al.*, Understanding the Preferential Oxidation of Carbon Monoxide (PrOx) Using Size-Controlled Au Nanocrystal Catalyst. *AIChE J.* **64**, 3159–3167 (2018).

31.	M. T. Bore, H. N. Pham, T. L. Ward, A. K. Datye, Role of pore curvature on the thermal stability of gold nanoparticles in mesoporous silica. *Chem. Commun.*, 2620–2621 (2004).

32.	Y. Chi, H. Lin, C. Mou, CO oxidation over gold nanocatalyst confined in mesoporous silica. *Appl. Catal. A Gen.* **284**, 199–206 (2005).

33.	X. Cao, *et al.*, Abnormal thermal stability of sub-10 nm Au nanoparticles and their high catalytic activity. *J. Mater. Chem. A* **7**, 10980–10987 (2019).

34.	W. Yuan, *et al.*, Direct In Situ TEM Visualization and Insight into the Facet-Dependent Sintering Behaviors of Gold on TiO 2. *Angew. Chemie - Int. Ed.* **57**, 16827–16831 (2018).

35.	A. D. Benavidez, *et al.*, Environmental Transmission Electron Microscopy Study of the Origins of Anomalous Particle Size Distributions in Supported Metal Catalysts. *ACS Catal.* **2**, 2349–2356 (2012).

36.	C. Radloff, N. J. Halas, Enhanced thermal stability of silica- encapsulated metal nanoshells. *Appl. Phys. Lett.* **79**, 674–676 (2001).

37.	C. Lin, X. Liu, S. Wu, K. Liu, C. Mou, Corking and Uncorking a Catalytic Yolk-Shell Nanoreactor: Stable Gold Catalyst in Hollow Silica Nanosphere. *J. Phys. Chem. Lett.* **2**, 2984–2988 (2011).

38.	J. Chen, R. Zhang, L. Han, B. Tu, D. Zhao, One-pot synthesis of thermally stable gold @ mesoporous silica core – shell nanospheres with catalytic activity. *Nano Res.* **6**, 871–879 (2013).

39.	P. Wynblatt, N. A. Gjostein, Particle growth in model supported catalysts-i. theory. *Acta Metall.* **24**, 1165–1174 (1976).